ACS APPLIED MATERIALS & INTERFACES

Research Article

www.acsami.org

Rational Design of Cancer-Targeted BSA Protein Nanoparticles as Radiosensitizer to Overcome Cancer Radioresistance

Yanyu Huang, Yi Luo, Wenjie Zheng, and Tianfeng Chen*

Department of Chemistry, Jinan University, Guangzhou 510632, China

Supporting Information

ABSTRACT: Radiotherapy displays curative potential for cervical cancer management, but radioresistance occurs during long-term therapy. To overcome this limitation, tumor-targeted nanotechnology has been proposed to enhance the radiosensitivity of solid tumors. Herein, we used biocompatible bovine serum albumin nanoparticles (BSANPs) as carriers of organic selenocompound (PSeD) with folate (FA) as the targeting ligand to fabricate a cancer-targeted nanosystem. The combination of PSeD and BSANPs endowed the nanosystem with higher light absorption and reactive oxygen species (ROS) generation owing to their properties of surface plasmon resonance (SPR) effect, heavy metal effect, high refractive index and nanoparticulate interfacial effect. The combined treatment drastically increased the ROS overproduction, VEGF/VEGFR2 inactivation and inhibition of XRCC-1-mediated repair of DNA damage, thus triggering G2/M phase arrest and apoptosis. Taken together, our findings demonstrate the utility of FA-BSANPs as a promising radiosensitizer to improve cancer radiotherapy.

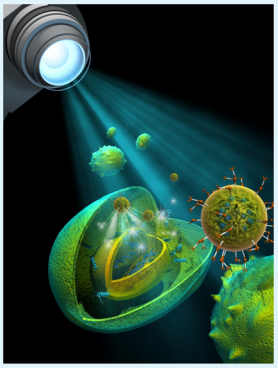

KEYWORDS: *bovine serum albumin nanoparticles, cancer-targeted nanosystem, folate, radiosensitization, radiotherapy*

INTRODUCTION

Radiotherapy has been extensively applied in noninvasive cancer treatment. Clinically, high energy X-ray or γ-ray techniques are used in radiotherapy to suppress tumor proliferation through causing DNA damage or free radical damage in tumor sites.[1−3] However, due to the differences in individual radiosensitivity and the limitation of irradiative dosage, some patients may suffer cancer recurrence and have poor therapeutic effects after radiotherapy. Besides, irradiative side effects caused by the poor discrimination between normal and tumor surrounding tissues limits the clinical implementation of radiotherapy. Moreover, cancer cells in lung, cervix, etc. undergoing radiation may trigger underlying molecular repair processes and finally lead to radioresistance.[4,5] Therefore, the development of new effective protocol for enhancing tumor radiosensitivity without compromising normal cell viability becomes an urgent priority. Currently, the combined use of chemotherapy and radiotherapy is considered as an effective strategy for radiosensitization. Recently, chemical therapeutics such as cisplatin and paclitaxel have been developed to be used as radiosensitizers to enhance cancer cells' sensitivity to radiation for lung, cervical, gastric, head and neck cancers.[6−8]

Selenium (Se) is a trace element with essential benefits for humans and animals. Numerous studies have shown that selenocompounds have excellent chemopreventive and chemotherapeutic effects in cancer treatment.[9,10]Among them, organoselenium compounds show higher absorption efficacy, better anticancer activity and lower toxicity comparing to inorganic Se forms in our previous studies.[11−14] Among these organic selenadiazole compounds, phenylbenzo [1, 2, 5] selenadiazole derivatives (PSeD) are identified to have strong anticancer abilities against different kinds of cancer and have little effect on normal cells. What's more, PSeD, as a semiconducting material, has metalloid properties, e.g., surface plasmon resonance (SPR) effect, heavy metal effect and high refractive index, which facilitate light absorption.[15] Therefore, PSeD is considered to be a promising radiosensitizer due to its high optical absorption. Despite this potency, the poor water-soluble ability and weak selective cytotoxicities of PSeD block its effective and precise accumulation in tumor sites. To achieve high therapeutic outcomes, a high dosage of free PSeD is needed, which can inevitably result in undesirable toxicity. Therefore, there has been intense interest in developing new types of drug delivery vehicles of PSeD for radiosensitization without compromising systemic viability.

Nanotechnology is considered as a promising strategy for cancer diagnostics, owing to its smart, sophisticated and multifunctional applications in tumor-targeted drug delivery and drug localization.[16−20] Nanoparticles provide customizable and selective drug delivery in tumor sites able to ferry effective amounts of chemotherapeutic agents while sparing normal cells.[21−23] Among them, albumin nanoparticles are considered as one of the biodegradable nanopayloads with easy functionalization for cancer therapy.[24,25] Indeed, Zhang et al. found out that bovine serum albumin nanoparticles (BSANPs)/poly(ethylene glycol) modified polyethylenimine (PEI−PEG) as a carrier of BMP-2 significantly enhanced de novo bone formation and drastically reduced PEI-caused NP toxicity.[26]

Received: August 5, 2014
Accepted: October 14, 2014
Published: October 14, 2014

Moreover, Mohanta et al. and Xie et al. respectively reported that surface decoration of chitosan on BSANPs contributed to drug-controlled release in response to pH changes.[27,28] Recently, researchers found out that the targeted ligand conjugation conferred the albumin nanoparticles to remarkable cytotoxicities against various cancer cells or even in xenografted nu/nu mouse.[29] However, the tumor-targeting BSANPs delivery system used as a chemical sensitizing agent for radiosensitization has been marginal.

Generally, expression of folate receptors (FARs) on normal cells is low, but the demand for FARs increases when the cells undergo cellular activation, proliferation and cells under malignant transformation.[30] Hela cervical cells overexpressing FARs are considered as radioresistant malignant cancer cells because they express pro-survival cytokines such as X-ray repair cross complementing protein 1 (XRCC-1), vascular endothelial growth factor (VEGF) and vascular endothelial growth factor receptor 2 (VEGFR2) to favor tumor progression and acquire treatment resistance after radiation.[31,32] Therefore, in this study, we chose folate (FA) as a targeting ligand to fabricate cancer-targeted BSANPs formulation as a drug delivery system for PSeD and, meanwhile, assessed its selective cytotoxicity as an important indicator for being a potential radiosensitizer. Besides, Hela cervical cells were selected as an X-ray-resistant cell model to determine the sensitizing capacity of FA-BSANPs in radiotherapy and the underlying action mechanisms.

EXPERIMENTAL METHODS

Materials. Phenylbenzo [1, 2, 5] selenadiazole derivatives (PSeD) were synthesized as previously described.[13,14] Folate (FA), *N*-(3-(dimethylamino)propyl)-*N*-ethylcarbodiimide (EDC) and glutaraldehyde 25% solution were purchased from Aladdin. Bovine serum albumin (BSA, fraction V, purity 95−99%), MTT and PI were obtained from Sigma-Aldrich. A bicinchoninic acid (BCA) kit was obtained from Thermo Fisher Scientific Inc. A terminal deoxynucleotidyl transferase dUTP nick end labeling (TUNEL) assay kit was purchased from Roche Applied Science. Dulbecco's modified Eagle's medium (DMEM) medium and fetal bovine serum (FBS) were purchased from NQBB International Biological Corporation. Milli-Q water was used in all experiments. An Elekta Precise linear accelerator was used as the radiotherapy instrument.

Preparation of FA-BSANPs. BSANPs were prepared using a desolvation technique as previously described with little modification.[29] Briefly, 40 mg of BSA powder dissolved in 2 mL of Milli-Q water was titrated to pH 8.2 using 0.1 N sodium hydroxide (NaOH), followed by dropwise addition of 8 mL of ethanol under stirring (800 rpm) at a rate of 1 mL/min. After the desolvation process, the nanoparticles were formed. Then 23.5 uL of 8% glutaraldehyde was slowly added, and the solution was allowed to stir for 24 h to cause particle cross-linking. To remove free BSA and glutaraldehyde, the prepared nanoparticles were purified by two rounds of centrifugation (12000 rpm, 20 min). The pellet was redispersed to the original volume in water under ultrasonication over 10 min. For FA conjugation, FA was activated with EDC. Briefly, 20 mg/mL of FA solution (dissolved in 0.1 N NaOH solution) was first reacted with EDC solution at a molar ratio of 1:5. The reaction was performed in dark with constant stirring for 2 h. Subsequently, the activated FA solution was dropwise added to BSANPs solution to form FA-conjugate BSANPs. Finally, PSeD solution (300 uL, 12.5 mg/mL) was added to FA-conjugated BSANPs under constant stirring at a time period of 24 h for incorporating PSeD. The FA-BSANPs was purified by three rounds of centrifugation (12000 rpm, 20 min) to remove unloaded PSeD, FA and EDC. The Se content in the nanosystem was calculated by inductively coupled plasma atomic emission spectroscopy (ICP-AES). The whole process was performed at room temperature.

Characterization of FA-BSANPs. The morphology of FA-BSANPs was determined by transmission electron microscopy (TEM, Hitachi H-7650), scanning electron microscopy (SEM, EX-250 system, horiba) and atomic force microscopy (AFM, Bioscope Catylyst Nanoscope-V). Fourier transform infrared spectroscopy (FTIR, Equinox 55 IR spectrometer) was used to characterize the structure information on FA-BSANPs in the range of 400−4000 cm^{-1}. The size distribution and ζ-potential of particles were monitored by Malvern Zetasizer Software.

Cell Culture and Determination of Cell Viability. In this paper, Hela cervical carcinoma cells, MCF-7 breast adenocarcinoma cells, A375 melanoma cells and L02 human hepatic cells were the human cell lines, which were applied from American Type Culture Collection (ATCC, Manassas, VA). These cell lines were maintained in DMEM medium with 100 units/mL penicillin, 10% fetal bovine serum and 50 units/mL streptomycin at 37 °C in 5% CO_2 incubator. FA-BSANPs-caused cell proliferative inhibition against various cell lines was measured by clonogenic assay.[33] and MTT assay.[34]

Determination of FA-BSANPs Cellular Uptake and Intracellular Trafficking. Intracellular uptake of FA-BSANPs in Hela and L02 cells was quantified by determining Se concentration using ICP-MS. Briefly, Hela and L02 cells were treated with different concentrations of FA-BSANPs with or without radiation (8 Gy) for different time periods, followed by cell digestion and redispersion. After that, the cells were counted and lysed using a hydrogen nitrate (HNO_3) and perchloric acid ($HClO_4$) mixture (HNO_3:$HClO_4$ = 3:1). Finally, the lysis solution was diluted with water to a volume of 10 mL. ICP-MS determination was performed to detect Se concentration, which quantified the uptake efficiency of internalized nanoparticles. The intracellular trafficking of FA-BSANPs in Hela and L02 cells was monitored using fluorescence imaging technique under fluorescence microscope (IX51, Olympus).[35]

Folate Competing Assay. The binding efficiency of FARs between FA-BSANPs and excessive FA was compared as previously described.[35] The internalized FA-BSANPs was quantified by the fluorescence intensity from PSeD under fluorescence microplate reader (Bio-Tek) (excitation wavelength at 482 nm and emission wavelength at 526 nm).

In Vitro Drug Release of FA-BSANPs. Four copies of FA-BSANPs radiated with 0 and 8 Gy were respectively dispersed in phosphate buffered saline (PBS) solution at a concentration of 1 mg/mL at acidic lysosomal (pH 5.3) and neutral blood (pH 7.4) environments. The solutions were kept in the dark at 37 °C to imitate in vivo environment. 250 μL of buffer was taken out and fresh buffer of the same volume was supplied. The release rate of PSeD was represented by its fluorescence intensity using a fluorescence microplate reader (excitation wavelength at 482 nm and emission wavelength at 526 nm).

Flow Cytometry. The cell cycle distribution after the treatment of FA-BSANPs and X-ray was measured by flow cytometric analysis.[36] The cells incubated with FA-BSANPs and X-ray were digested, collected and centrifuged at a speed of 1500 rpm for 10 min. The harvested cells were fixed with 70% ethanol at −20 °C overnight followed by PI staining. The DNA contents were quantified by the fluorescence intensity of PI. The cell samples were analyzed on a Beckman Coulter Epics XL MCL flow cytometer (Beckman Coulter, Inc., Miami, FL). The DNA histogram represented the cell number in G0/G1, S and G2/M phases, while the sub-G1 peak quantified the hypodiploid DNA number in apoptotic cells. The DNA contents of the cell samples were analyzed by MultiCycle software (Phoenix Flow Systems, San Diego, CA);

TUNEL and 4′,6-Diamidino-2-phenylindole (DAPI) Staining Assay. FA-BSANPs-caused DNA fragmentation was confirmed by TUNEL assay in Hela cells. Briefly, the cells attached in 2 cm dishes were fixed and permeabilized with 3.7% formaldehyde and 0.1% Triton-X solution, respectively. After that, TUNEL working buffer and DAPI were added for cell staining. The morphology of stained cells was observed under a fluorescence microscope (EVOS FL auto, Life Technologies, Grand Island, NY).

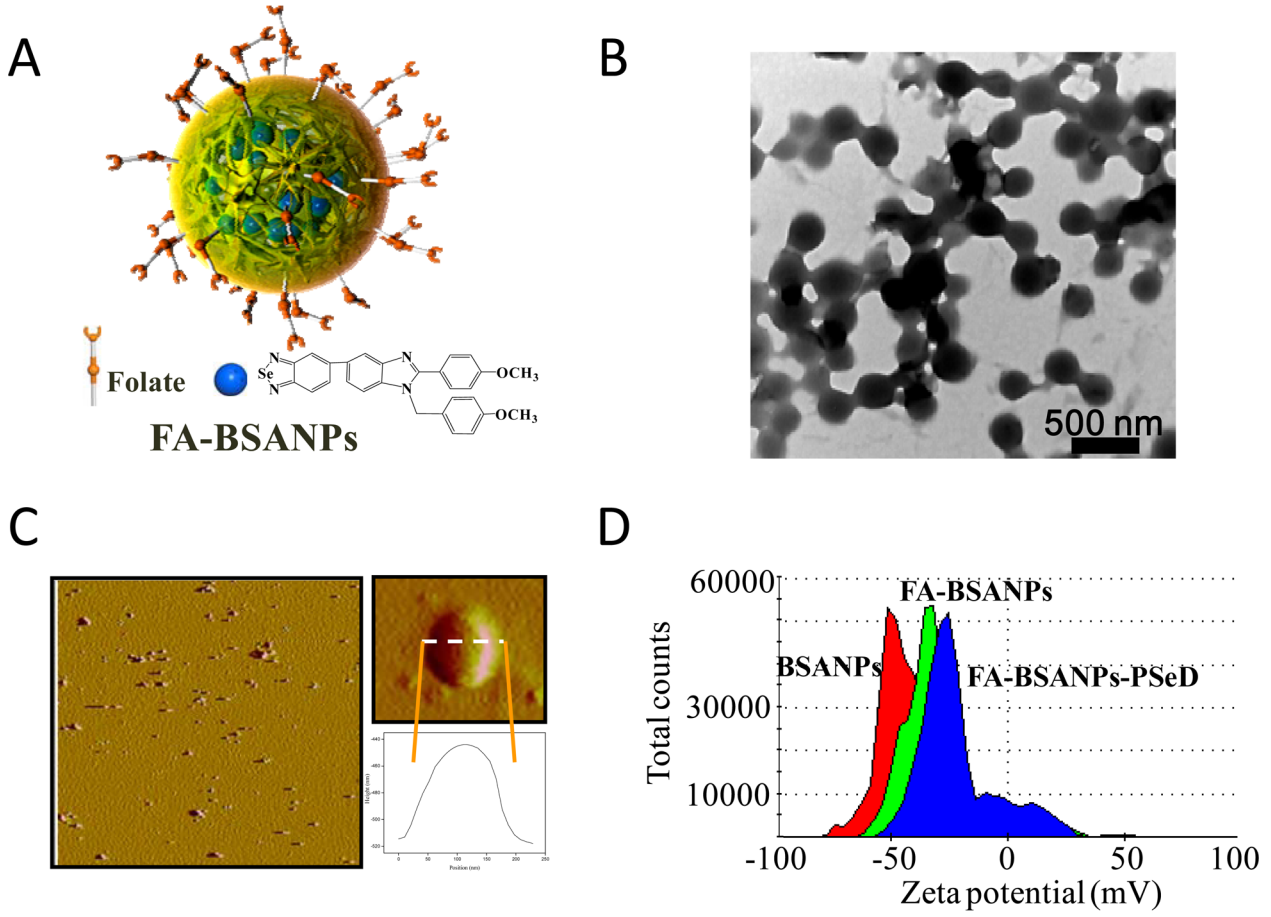

Figure 1. Chemical properties of FA-BSANPs. (A) Structure depiction of FA-BSANPs. (B) TEM image of FA-BSANPs, scale bar =500 nm. (C) AFM image of FA-BSANPs and roughness analysis of individual nanoparticle. The surface roughness of individual nanoparticle was examined by AFM Nanoscope Analysis Software. (D) δ-potential of BSANPs, FA-BSANPs and FA-BSANPs-PSeD.

Determination of Reactive Oxygen Species (ROS) Generation. Changes of intracellular ROS generation caused by FA-BSANPs with or without radiation were evaluated using dihydroethidium (DHE, Beyotime) and a 2′,7′-dichlorofluorescin diacetate (DCFDA) probe, respectively. Briefly, Hela cells pretreated with different concentrations of FA-BSANPs for 2 h were irradiated at a dosage of 0, 8 Gy, respectively. At the end of radiation, the cells were stained with 10 μM DHE at the final concentration and DCFDA at 37 °C for 30 min. The cells were rinsed with PBS twice and incubated in fresh PBS. The fluorescence intensity of DHE and DCF (excitation and emission wavelength at 300 nm/610 and 488 nm/525 nm, respectively) quantified the intracellular ROS level. For the determination of extracellular ROS generation caused by FA-BSANPs and free PSeD, DHE staining assay was conducted in PBS without cells.

Western Blot Analysis. The expression of proteins involved in signaling pathways after combined treatment of FA-BSANPs and radiation in Hela cells and L02 cells were determined by Western blot analysis. Briefly, the cells were lysed with RIPA buffer and the total proteins were obtained from supernatant after centrifugation (12000 rpm) at 4 °C. The proteins were quantified using BCA assay. After that, SDS-PAGE was performed with equivalent amount of proteins loading. Subsequently, the separated proteins were transferred to PVDF membranes, blocked with 5% nonfat milk, incubated with primary antibodies and second antibodies-conjugated horseradish peroxidase, and were finally visualized on X-ray films.

Statistical Analysis. All experiments were performed at least for 3 times and the data in this study was expressed as means ± SD. Statistical significance of the data were analyzed by SPSS statistical program (Version 13, SPSS Inc., Chicago, IL). Difference between two groups was calculated by two-tailed Student's *t*-test. Variation with $P < 0.05$ (*) or $P < 0.01$ (**) was considered statistically significant. The difference between three or more groups was analyzed by one-way ANOVA multiple comparisons.

RESULTS AND DISCUSSION

Design, Preparation and Characterization of FA-BSANPs. In this study, we reported a cancer-targeted nanosystem FA-BSANPs as biocompatible and effective sensitizer for radiosensitization. FA-BSANPs was fabricated through conjugation of FA and loading of organic selenocompound PSeD to BSANPs (Figure 1A). The morphology of FA-BSANPs was detected and analyzed using various microscopic methods. TEM imaging (Figure 1B) and SEM imaging (Figure S1, Supporting Information) showed that the as-prepared FA-BSANPs was spherical in shape and well cross-linked. The surface roughness of FA-BSANPs was examined by AFM morphological analysis (Figure 1C). The AFM image of the single nanoparticle and its corresponding analytical curve commonly demonstrated the smooth surface of FA-BSANPs. The stability of FA-BSANPs is of importance for its medical use and storage. Therefore, the size of FA-BSANPs in aqueous solution was monitored for 37 days. As shown in Figure S2 (Supporting Information), the average size of FA-BSANPs in aqueous solution kept stable with the average size at 255 nm for 37 days. The average size of FA-BSANPs in PBS solution remained at 355 nm within 5 days, following a gradual size increase to 470 nm after 12 days. Even though the

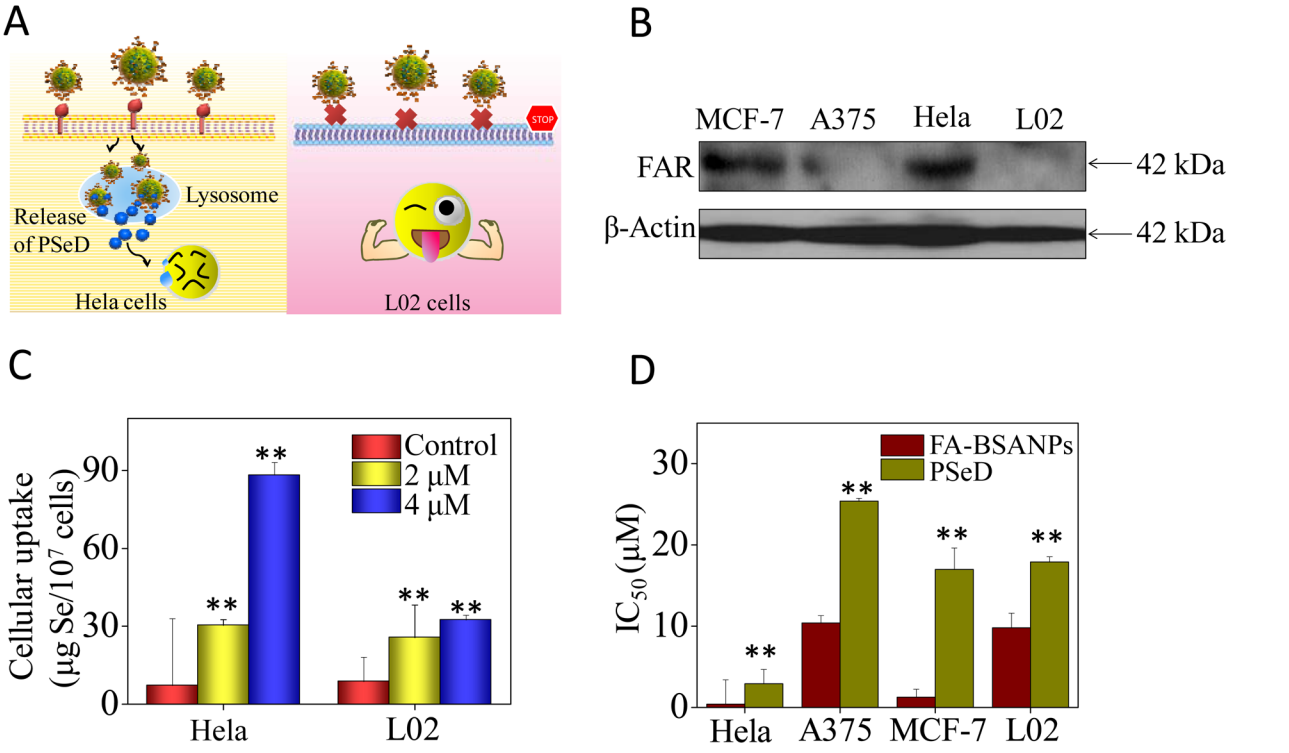

Figure 2. Selective cellular uptake and selective cytotoxicity of FA-BSANPs. (A) Proposed selective cellular uptake of FA-BSANPs between Hela cells (folate receptors overexpressed) and L02 cells (hardly expressed folate receptors). (B) Folate receptors (FARs) expression in Hela cells, A375 cells, MCF-7 cells and L02 cells. The expression level of FARs was evaluated by Western blot analysis. β-Actin was used as loading control. (C) Quantitative determination of cellular uptake of FA-BSANPs in Hela cells and L02 cells. Hela cells and L02 cells were treated with FA-BSANPs for 4 h, respectively. Se concentration was measured by ICP-MS analysis. *$P < 0.05$ vs control, **$P < 0.01$ vs control. (D) Proliferative inhibition of FA-BSANPs against MCF-7 cells, A375 cells, Hela cells and L02 cells for 72 h. * and ** indicate significant difference between PSeD and FA-BSANPs group at $P < 0.05$ and $P < 0.01$ levels, respectively. Values expressed were means ± SD of triplicate.

nanoparticles in PBS tended to aggregate, it is still safe for their medial use. The reason for that is the half-life period of serum albumin is not exceeding 10 days, therefore the FA-BSANPs will be eliminated out the body before it aggregates to over 470 nm. Figure S3 (Supporting Information) applies detailed information for the size distribution of FA-BSANPs in aqueous and PBS solution. Furthermore, the ζ-potential changes of nanoparticles were recorded while new component was added to the nanoparticulate system. As shown in Figure 1D, the ζ-potentials of plain BSANPs were −51.8 mV. After FA conjugated and PSeD loaded on BSANPs, the ζ-potential of FA-BSANPs and FA-BSANPs-PSeD was turned to −31.6 and −22.5 mV, respectively.

The chemical structure of FA-BSANPs was examined by FT-IR spectra. As shown in Figure S4 (Supporting Information), the BSANPs spectrum (line c) at 2926 cm^{-1} was its characteristic peak; the peaks at 1650 and 1538 cm^{-1} presented the first and secondary -CO−NH- groups from BSANPs. In the spectrum of FA-BSANPs (line b), the peaks at 1510 and 1447 cm^{-1} were assigned to the benzene rings from FA (line b, Figure S5, Supporting Information). Specifically, the peak of amide groups in line b was stronger, indicating that new amide groups were formed between carboxylate groups from activate FA and amino groups on the surface of BSANPs. In the spectrum of FA-BSANPs-PSeD (line c), the 1257 cm^{-1} was assigned to the $-OCH_3$ groups of PSeD (line a, Figure S5, Supporting Information).

Selective Accumulation of FA-BSANPs in Cancer Cells. Specific ligand-guiding delivery is necessary for chemical radiosensitizer to achieve successful and selective tumor-targeting. Therefore, we need to ensure precise amount of FA-BSANPs accumulated in tumor site without exploiting normal cells viability before the radiation study. In this case, we quantified the selective cellular uptake of FA-BSANPs in different cell lines, namely Hela cells overexpressing FARs and L02 cells that hardly expressed FARs (Figure 2A, B). Cells seeded in 10 cm dishes were incubated with 2 and 4 μM FA-BSANPs for 4 h; the cellular uptake of FA-BSANPs was measured by determining Se concentration using ICP-MS. As depicted in Figure 2C, the uptake amount of FA-BSANPs in Hela cells was much higher than that in L02 cells. For instance, after 4 h of incubation with 4 μM FA-BSANPs in Hela cells, the internalized FA-BSANPs amount was 2.7-fold higher than that in L02 cells.

To confirm the role of FA-guiding delivery, FA competing assay was performed. Briefly, Hela cells were pretreated with excess amount of FA to block FARs on cell membranes, then were incubated with FA-BSANPs for drug internalization. Figure S6 (Supporting Information) clearly shows that excess amount of FA dose-dependently blocked the cellular uptake of FA-BSANPs, which suggests that FA/FARs-mediated endocytosis directly promoted the selective cellular uptake of FA-BSANPs in Hela cells.

To verify the antiproliferative ability of FA-BSANPs in different cell lines, MTT assay was performed. Figure 2D shows that FA-BSANPs exerted great cytotoxicities against Hela cells and MCF-7 cells, with IC_{50} values at 0.4 and 1.25 μM, respectively, whereas PSeD was less cytotoxic against these two

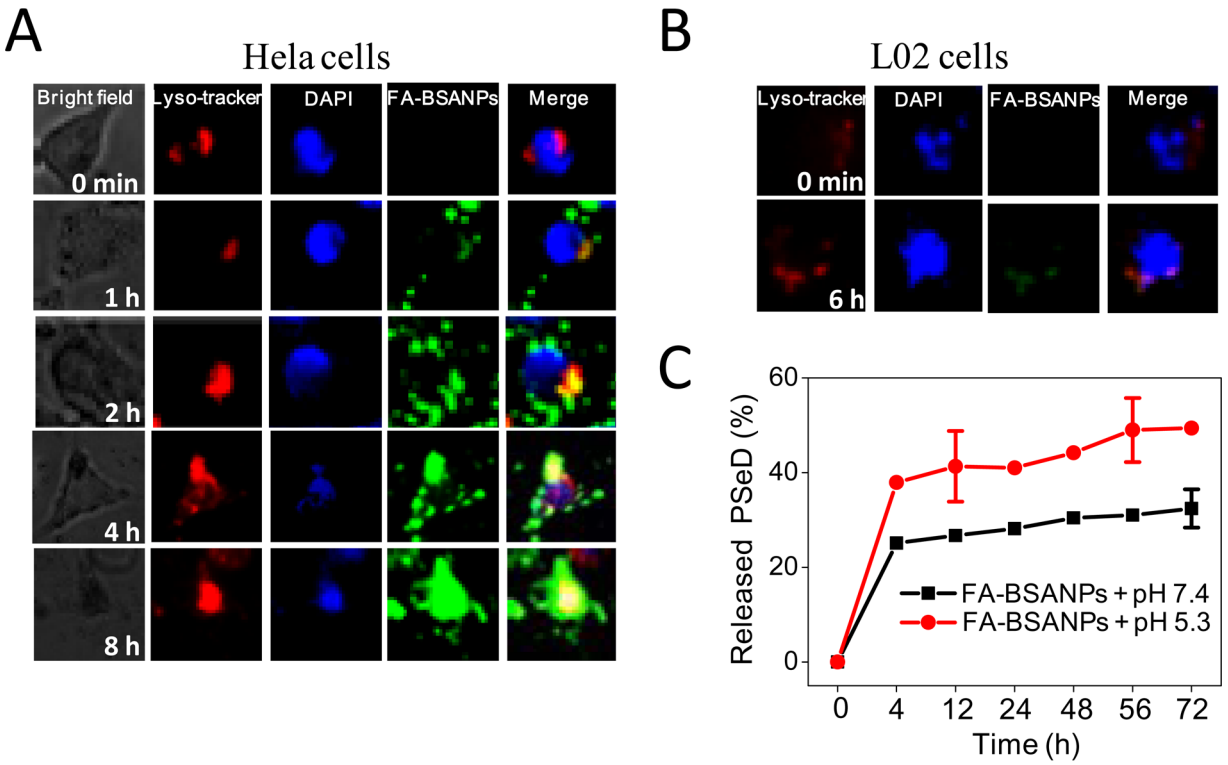

Figure 3. Internalization and release behavior of FA-BSANPs in Hela and L02 cells. (A) Intracellular trafficking of FA-BSANPs observed in individual Hela cell. (B) Intracellular trafficking of FA-BSANPs observed in individual L02 cell. Hela cells and L02 cells were treated with FA-BSANPs (80 μM) with DAPI and lyso-tracker staining at 37 °C. The cells incubated for 0 min, 1 h, 2 h, 4 and 8 h were observed under a fluorescent microscope. (C) In vitro release profiles of PSeD from FA-BSANPs with varied pH values. The solutions of FA-BSANPs were incubated in PBS solution with pH values at 5.3 and 7.4, respectively. The released PSeD concentrations were recorded by the fluorescent intensity of PSeD with the excitation and emission wavelengths at 482 and 526 nm, respectively, at certain periods of time. Values expressed were means ± SD of triplicate.

tumor cells, with IC_{50} values at 2.9 and 17 μM, respectively. These results revealed that FA-BSANPs was superior than free PSeD for suppressing tumor cells proliferation. Meanwhile, FA-BSANPs exerted 24 times lower cell growth inhibition against A375 and L02 cells with low FARs expression levels than FAR-overexpressing Hela and MCF-7 cells with IC_{50} values at 10.4 and 9.8 μM, respectively. Therefore, the FA/FARs-mediated targeting effect endows FA-BSANPs the selective cytotoxicity toward cancer cells.

To further understand the action of FA-BSANPs after internalization, we monitored FA-BSANPs intracellular trafficking under a fluorescence microscope. Hela cells and L02 cells were pretreated with lyso-tracker (red) and DAPI (blue) to stain lysosome and nucleus. Figures 3A and S7A (Supporting Information) displayed the time-course internalization of FA-BSANPs at the individual Hela cell level. At the time point of 1 h, FA-BSANPs moved across the Hela cell membrane and began to locate in the lysosome. After that, the green fluorescence of FA-BSANPs continuously aggregated in the lysosome and finally "saturated" the cytoplasm in the Hela cell at 8 h. In contrast, no green fluorescence was detected in nucleus through the observation, indicating that lysosome was the main target of FA-BSANPs after internalization rather than nucleus. Meanwhile, there was only a weak fluorescence observed in L02 cells, even after 6 h, which further demonstrated the lower uptake of FA-BSANPs in L02 cells (Figures 3B and S7B, Supporting Information). These results suggest that FA-BSANPs could selectively enter Hela cells and targeted lysosome for subsequent cellular actions.

In vitro drug release profiles of FA-BSANPs were examined in acidic (pH 5.3) and neutral (pH 7.4) PBS solutions to intimate its drug release behavior in blood and lysosome environments, respectively. Figure 3C shows that the accumulative release of PSeD amount at pH 5.3 reached 41.0% in 24 h and to 49.2% in 72 h, whereas at pH 7.4, the release amount of PSeD reached 28.2% in 24 h and 32.4% in 72 h. The much rapid release rate of PSeD from FA-BSANPs at pH 5.3 should be due to the acidolysis of nanoparticles. At pH 7.4, FA-BSANPs was well-organized, which blocked the release of PSeD, whereas FA-BSANPs at pH 5.3 was hydrolyzed in an acid environment, which led to BSANPs degradation and pushed PSeD release. This hydrolysis behavior of BSANPs in response to acid pH conferred this drug delivery system to the function of pH-controlled release of drugs.

Use of FA-BSANPs as Radiosensitizer for Radiotherapy. The biochemical experiments above have demonstrated that FA-BSANPs has an excellent anticancer ability and biocompatibility with minimal side effects. These properties of FA-BSANPs satisfied the basic need of being a radiosensitizer. Next, we conducted successive physical and biochemical experiments to determine whether FA-BSANPs could enhance the therapeutic effectiveness of radiotherapy. Clonogenic assay was conducted to evaluate the cell viability in Hela cells and L02 cells caused by the combination of X-ray and FA-BSANPs. As depicted in Figure 4A, single FA-BSANPs (4 μM) and X-ray (8 Gy) treatment decreased Hela cell colony formation to 67.1% and 55.7%, respectively, while FA-BSANPs and X-ray in combination drastically inhibited cell survival to 4.3%. In detail, the combined treatment of FA-BSANPs and X-ray radiation

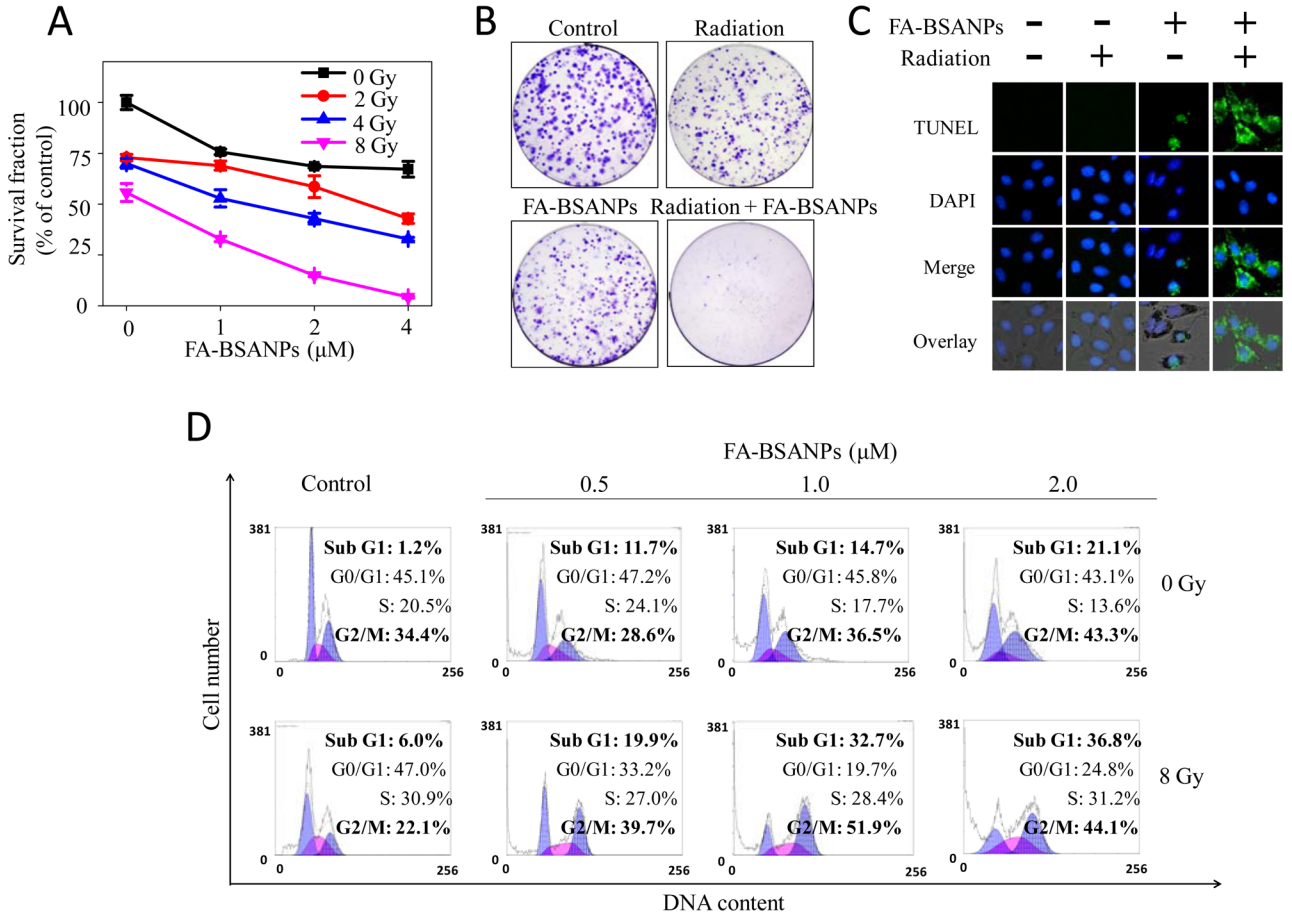

Figure 4. FA-BSANPs in combination with X-ray radiation increased G2/M phase arrest and apoptosis in Hela cells. (A) Combined treatment of FA-BSANPs and X-ray radiation decreased Hela cells survival detected by clonogenic assay. Hela cells were pretreated FA-BSANPs at different concentrations for 2 h and then were irradiated by X-ray radiation at different dosages. Values expressed were means ± SD of triplicate. (B) Colony formation of Hela cells under the cotreatment of FA-BSANPs and radiation (8 Gy). (C) Fluorescence images of DNA fragmentation and nuclear condensation after exposure to FA-BSANPs or/and X-ray radiation. Cells pretreated with FA-BSANPs (4 μM) and X-ray radiation (8 Gy) were stained with TUNEL working buffer and DAPI for DNA fragmentation and nucleus visualization, respectively. (D) Combined treatment of FA-BSANPs and X-ray radiation enhanced G2/M phase arrest and apoptosis in Hela cells. The cell cycle distribution after different treatments were analyzed by quantifying DNA content using flow cytometric analysis.

resulted in the decline of cell colony formation in a dose-dependent manner. The corresponding microscopic images displayed in Figure 4B evidenced the significant cytotoxicity of combined treatment against Hela cells. Similar results were obtained in MTT assay and corresponding microscopic images (Figure S8A,B, Supporting Information), which further demonstrated the radiosensitization caused by FA-BSANPs. Oppositely, in L02 cells, FA-BSANPs treatment alone slightly affected the colony formation, causing 29.2% cell growth inhibition at a concentration of 4 μM, whereas X-ray radiation alone (8 Gy) drastically reduced the colony formation to 27.51% in L02 cells. In contrast, pretreatment of the cells with FA-BSANPs increased the survival rate of L02 cells exposed to X-ray radiation (Figure S9A,B, Supporting Information). These results suggest that pretreatment of human normal cells with FA-BSANPs could antagonize the cell death caused by X-ray radiation.

Generally, the action mechanism of cell death included apoptosis and/or cell cycle arrest. We next determined the intracellular mechanism for FA-BSANPs + radiation-caused cells death using flow cytometry and TUNEL&DAPI staining methods (Figure 4C,D). As analyzed by flow cytometry (Figure 4D), radiation (8 Gy) alone slightly caused 22.1% of G2/M phase arrest, and FA-BSANPs (from 0.5 to 2 μM) activated apoptotic cell death from 11.7% to 21.1%, as reflected by the Sub G1 proportions. However, the combination of FA-BSANPs and radiation dose-dependently increased the extent of G2/M phase arrest and cell apoptosis. For instance, combination of FA-BSANPs (2 μM) and radiation at 8 Gy enhanced the proportions of G2/M phase arrest and Sub-G1 peak to 44.1% and 36.8%, respectively. The populations of Sub G1, G0/G1, S and G2/M phases in each group were also quantified as bar charts (Figure S10, Supporting Information). TUNEL and DAPI staining assay further evidenced the cell apoptosis after whole treatment. Figure 4C reveals that FA-BSANPs (4 μM) combined with radiation (8 Gy) displayed greater level of DNA fragmentation (green fluorescence) and nucleus condensation (blue fluorescence) than single treatment alone. These results further demonstrated the induction of apoptosis by FA-BSANPs and radiation.

Generally, apoptosis was executed via mitochondria-mediated (intrinsic) and death receptor-mediated (extrinsic) signaling pathways. The extrinsic pathway is activated by death receptors including Fas, TNF and TRAIL receptors.[37−39] while the intrinsic mitochondrial pathway is affected by Bcl-2 family proteins, which is affected by p53 phosphorylation and

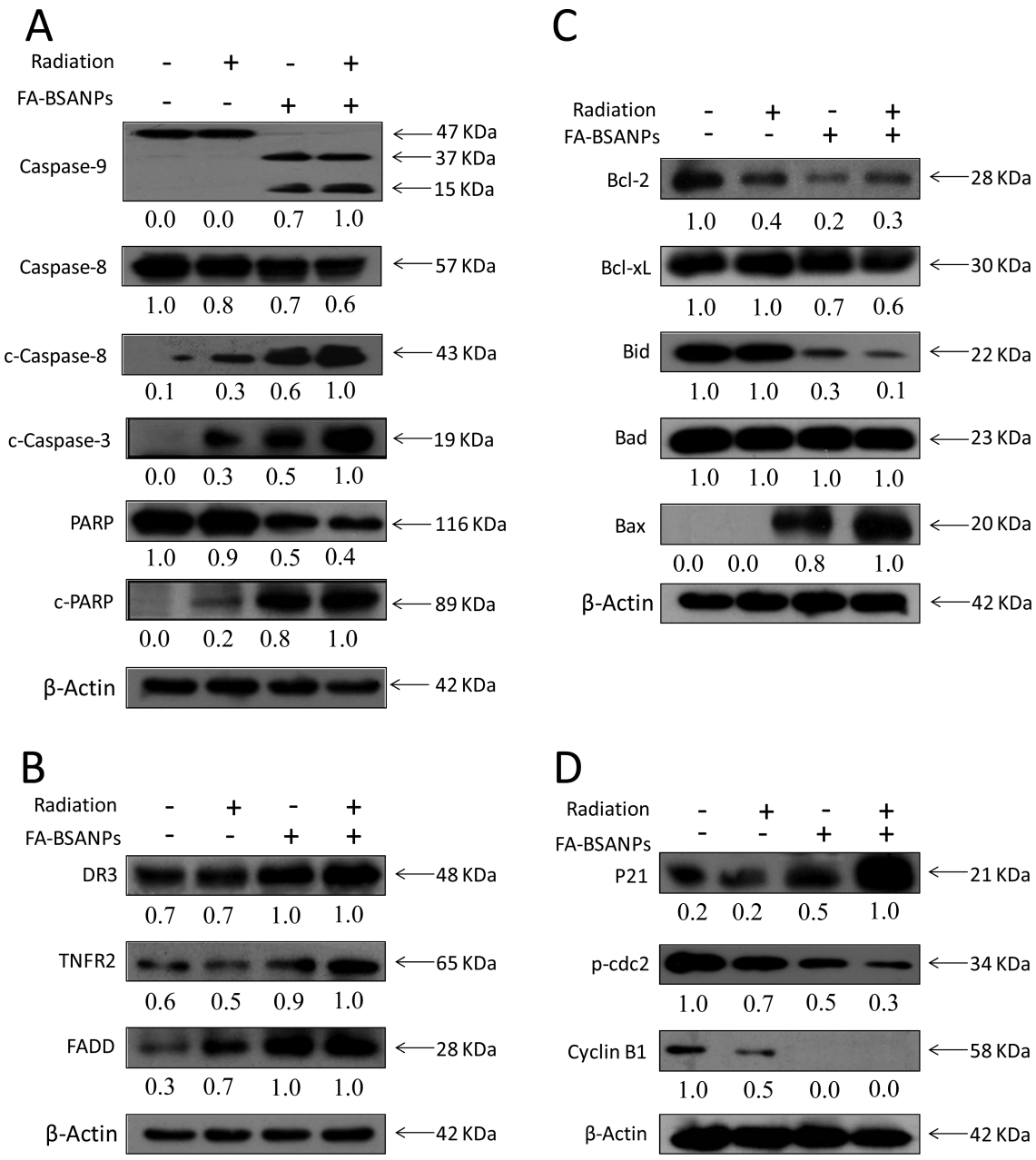

Figure 5. Combination of FA-BSANPs (4 μM) and X-ray radiation (8 Gy) enhanced the expression level of proteins related to G2/M phase arrest and apoptosis. Western blot analysis for the expression of (A) Caspase-8, c-Caspase-8, Caspase-9, c-Caspase-3, PARP, c-PARP; (B) DR3, TNFR2, FADD; (C) Bcl-2, Bcl-xL, Bid, Bad, Bax and (D) p21 Waf1/Cip (DCS60), p-cdc2 and Cyclin B1. β-Actin was used as the loading control.

activate downstream apoptotic signals.[40,41] Previous studies have demonstrated that a combination of radiation and radiosensitizers increased their anticancer efficacy with the involvement of caspase activation.[42,43] Consistently, in this study, we demonstrated that treatment of cells with X-ray radiation alone slightly induced Hela cell apoptosis, as evidenced by activation of caspase-3/-8/-9 and PARP cleavage (Figure 5A). Pretreatment of the cells with FA-BSANPs augmented the anticancer efficacy of X-ray radiation by triggering both intrinsic and extrinsic pathways, and finally exaggerated apoptotic signals, which was supported by higher levels of cleavage of caspase-3/8/9 and PARP (Figure 5A). Moreover, FA-BSANPs and radiation enhanced expression of extrinsic upstream proteins (DR3, TNFR2 and FADD) and intrinsic Bcl-2 family expression Bax, while down-regulated the expression of Bcl-2 and Bcl-xL (Figure 5B,C). Meanwhile, significant decrease in the expression level of total Bid was observed in cells exposed to the combined treatments, which indicate the cross-link between intrinsic and extrinsic apoptotic pathways.

On the basis of an observed G2/M phase arrest examined by flow cytometric determination, we evaluated the expression level of cdc 2 and cyclin B1, because the activation of cyclinB/CDK1 complex and cdc 2 mostly affected G2/M phase progression. As expected, Figure 5D displays a noticeable down-expression of cyclin B1 and phosphorylated cdc 2 in Hela cells after the combination of FA-BSANPs and radiation. Because p21 is a member of CDK inhibitors (CKDIs) associated with G2/M phase arrest, the intracellular p21waf1/Cip1 level was determined to be up-regulated, which inhibited

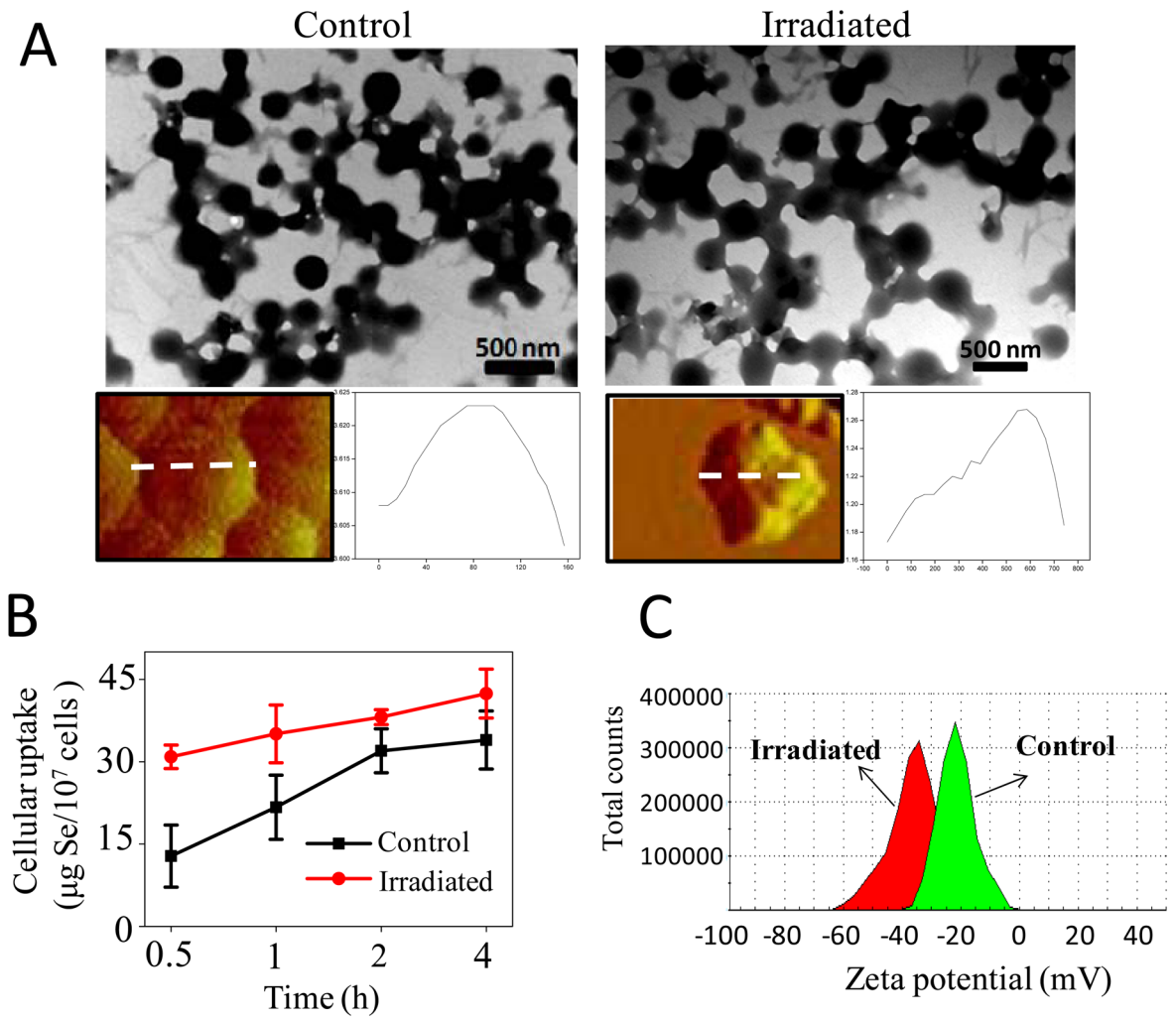

Figure 6. Changes of morphology, cellular uptake and ζ-potential of FA-BSANPs with or without radiation. (A) Morphology and surface roughness of FA-BSANPs with or without X-ray radiation (8 Gy) detected by TEM and AFM microscopic methods. Scale bar (TEM image) = 500 nm. The analytical profiles of FA-BSANPs' surface roughness were obtained using AFM Nanoscope Analysis Software. (B) Cellular uptake efficiency of FA-BSANPs (2 μM) with or without X-ray radiation (8 Gy) in Hela cells. Values expressed are means ± SD of triplicate. (C) ζ-potential changes of FA-BSANPs with or without radiation (8 Gy).

G2/M phase progression. Taken together, FA-BSANPs potentiated X- ray radiation to cause cell death with the involvement of apoptosis and G2/M phase arrest.

Furthermore, Western blot analysis was performed to examine the change in the expression levels of proteins related with apoptosis and G2/M phase arrest induced by FA-BSANPs and radiation in L02 cells. As shown in Figure S11 (Supporting Information), X-ray radiation alone affected the expression of apoptotic and G2/M phase arrest-related proteins, such as Bid, FADD, caspase-8/-9/-3, PARP and p21. Interestingly, compared with the X-ray group, although the combined treatment triggered the cleavage of caspase-8 and subsequent truncation of Bid, and increase in expression of Bax, a decrease in cell apoptosis proteins, cleaved caspase-3 and PARP was observed. FA-BSANPs also effectively reversed the effects of X-ray on p21. The interaction of these different signaling pathways may contribute to the protective effects of the nanoparticles on L02 cells against X-ray-induced damage.

Action Mechanisms of FA-BSANPs-Induced Radiosensitization. To understand the mechanism of FA-BSANPs-mediated radiosensitization, we investigated the physicochemical changes of FA-BSANPs with or without radiation. As a result, FA-BSANPs kept stable under X-ray radiation, as evident by negligible changes on FA-BSANPs' size, morphology (Figure 6A), distribution (Figure S12A,B, Supporting Information) and drug release behavior (Figure S13, Supporting Information). However, nanoparticles under irradiative conditions had roughened surfaces, as seen in AFM images and the uneven highness profiles of individual nanoparticles (Figures 6A and S14, Supporting Information). The roughened surface of FA-BSANPs enhanced FA-BSANPs to cell membrane adhesion, which potentially facilitated cellular uptake. To verify this appealing suggestion, we compared the uptake efficiency of FA-BSANPs with or without radiation in Hela cells. As shown in Figure 6B, the uptake amount of irradiated nanoparticles reached 45.2 μg Se/10^7 cells after 4 h of incubation, which was 1.3-fold higher than that of the nonradiated nanoparitcles (34.8 μg Se/10^7 cells). Taken together, these results demonstrated that X-ray radiation enhanced the surface roughness of FA-BSANPs, which enhanced the adhesion between FA-BSANPs and cell membranes, thereby increasing the cellular uptake of FA-BSANPs in Hela cells. Besides, the ζ-potential of FA-BSANPs was changed from −21.5 to −34.6 mV after irradiation

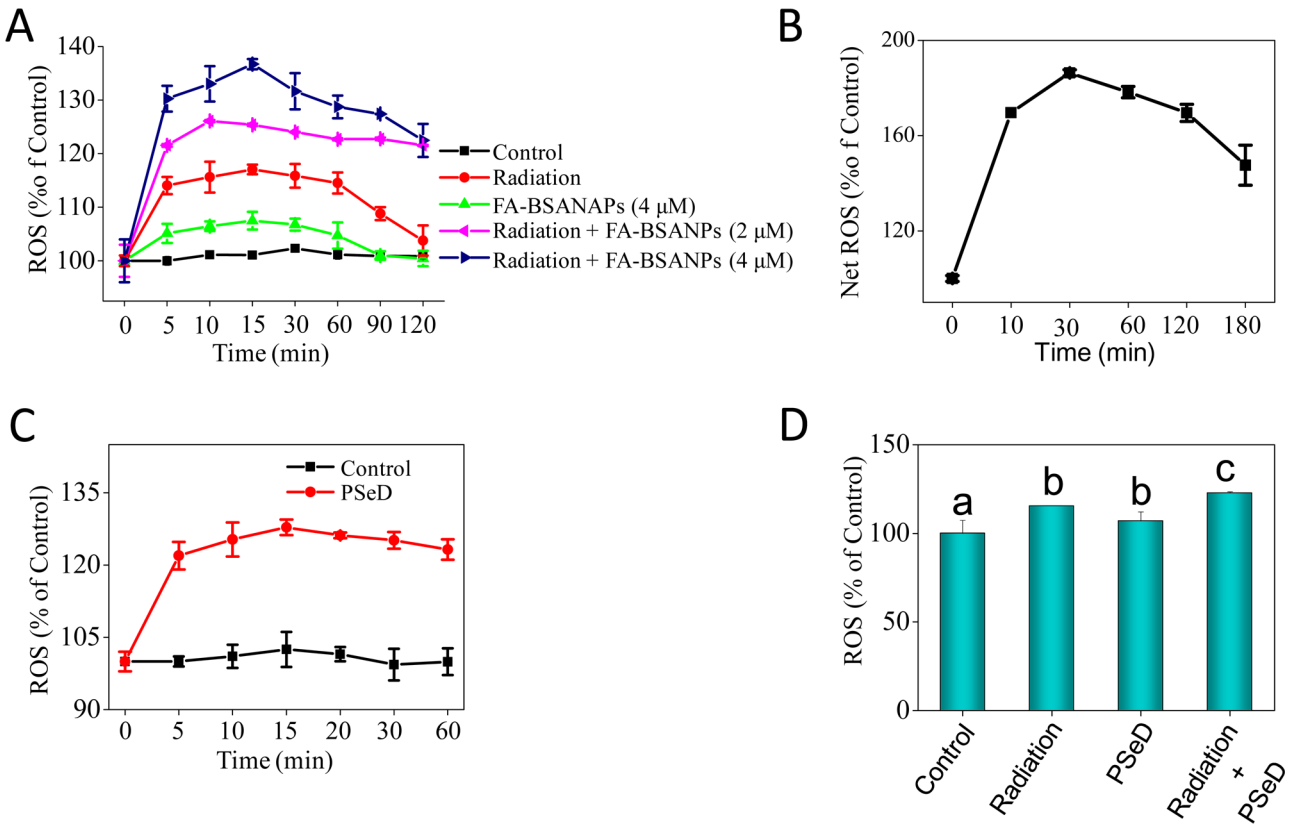

Figure 7. Changes in ROS generation induced by cotreatment of FA-BSANPs and X-ray radiation. (A) ROS generation induced by FA-BSANPs or/and X-ray radiation in Hela cells. Cells pretreated with different concentrations of FA-BSANPs were treated with 8 Gy of X-ray radiation and were finally incubated with 10 μM DHE for 30 min. (B) ROS generation induced by FA-BSANPs under X-ray radiation in PBS solution. FA-BSANPs (4 μM) irradiated by X-ray radiation (8 Gy) were incubated with DHE at a concentration of 10 μM for 30 min. (C) ROS generation induced by PSeD + X-ray radiation in Hela cells. Hela cells pretreated with 4 μM PSeD before exposure to 8 Gy of X-ray radiation were finally incubated with 10 μM DHE in PBS for 30 min. (D) ROS generation induced by PSeD with or without radiation in PBS solution. 4 μM PSeD irradiated by 8 Gy of radiation were incubated with 10 μM DHE in PBS at 37 °C for 2 h. The ROS level was quantified as the fluorescence intensity of DHE. Values represented are means ± SD of triplicates. Bars with different characters are statistically different at the $P < 0.05$ level.

(Figure 6C), which further confirms that X-ray treatment could change the physicochemical properties of FA-BSANPs.

It has been reported that radiosensitizers could enhance the anticancer efficacy of radiotherapy through generating radiochemicals, e.g., free radicals and ionizations when irradiated, therefore increasing the intracellular ROS level that cause DNA damage in cancer cells.[44−46] Therefore, we detected whether FA-BSANPs were able to potentiate radiation for ROS overproduction by using DHE and DCFDA fluorescent probes. Figure 7 displays the overproduction of ROS level under combined treatment using a DHE probe. As displayed in Figure 7A, the treatment of FA-BSANPs and radiation significantly triggered intracellular ROS overproduction in Hela cells. To verify this synergistic effect of FA-BSANPs, a cell-free model was performed. Figure 7B shows that FA-BSANPs in an extracellular environment overproduced the ROS level to 186.3% in 30 min after being irradiated. This should be ascribed to the nanoparticulate interfacial effect of FA-BSANPs in response to radiation.[47] Apart from FA-BSANPs, the action of PSeD should be a contributing factor for ROS overproduction. Therefore, we conducted DHE determination to assess whether PSeD could induce ROS overproduction. As shown in Figure 7C, PSeD up-regulated intracellular ROS level to 127.8% in 15 min. Besides, PSeD being irradiated outside the cells produced higher ROS generation than a single agent alone at 2 h after radiation (Figure 7D), indicating that PSeD could also synergize with radiation to enhance ROS generation. Because PSeD as the organic Se form has metalloid properties, namely surface plasmon resonance (SPR) effect and heavy metal effect, which facilitate light absorption, the enhanced ROS level should be attributed to the efficient absorption of X-ray caused by PSeD. The results of DCFDA probe analysis also confirmed the above finding that PseD could synergize with radiation to enhance ROS generation (Figure S15, Supporting Information).

To understand the intracellular radiosensitizing mechanism of FA-BSANPs, we determined the signaling pathway caused by FA-BSANPs and radiation in combination (Figure 8). As described before, VEGF/VEGFR2 and XRCC-1 are highly expressed in X-ray resistant cervical cells and are responsible for DNA repair and proliferative protection after radiation damage. Therefore, we used Western blot analysis to determine whether the expression of VEGF/VEFGR2, XRCC-1 can be exploited by the cotreatment of FA-BSANPs and radiation. As shown in Figure 8B, pretreated FA-BSANPs drastically inhibited X-ray-caused VEGF/VEGFR2 and XRCC-1 overexpression, indicating that the addition of FA-BSANPs successfully reversed X-ray resistance in Hela cells. These results demonstrate that VEGF/VEGFR2 and XRCC-1 could be the molecular targets of FA-BSANPs to overcome the radioresistance of cancer cells.

p53 is a key tumor suppressor responsible for oxidative stress and could modulate different cellular events including cell cycle

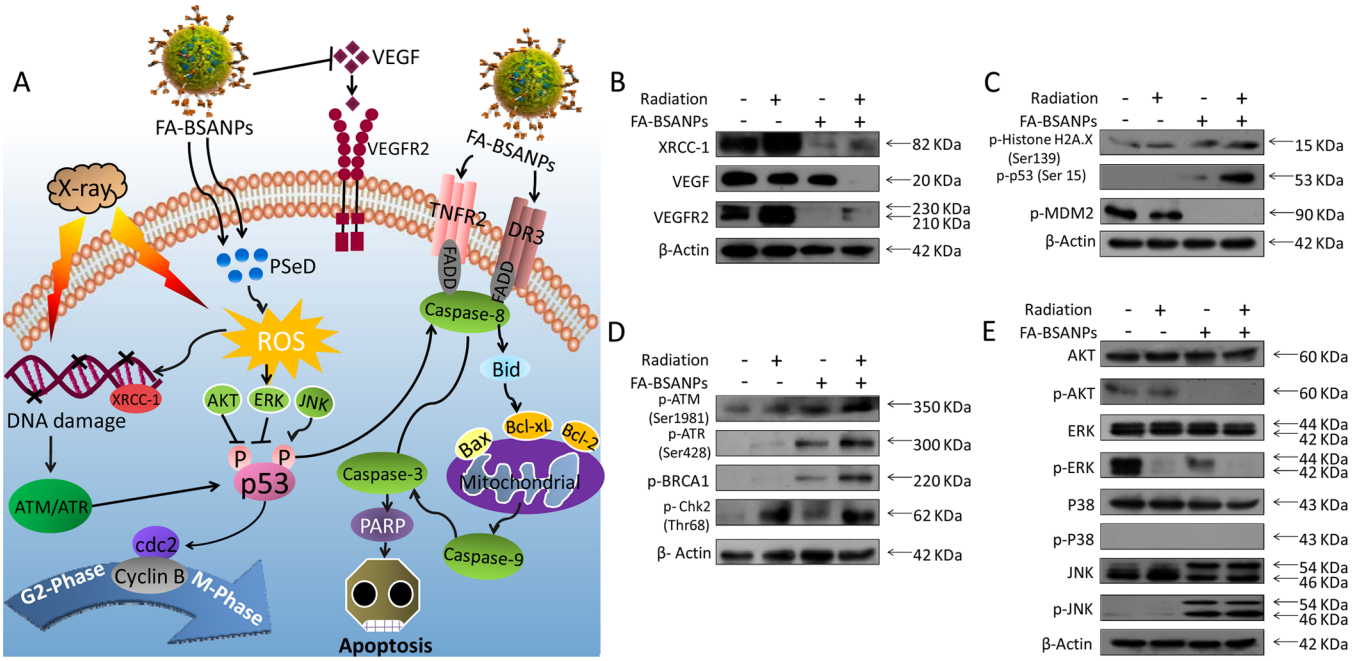

Figure 8. Signaling pathways triggered by FA-BSANPs and X-ray radiation. (A) Overview of G2/M phase arrest and apoptosis signaling pathway caused by FA-BSANPs and X-ray radiation in combination in Hela cells. Western blot analysis for the expression of (B) XRCC-1, VEGF, VEGFR2; (C) p-Histone, p-p53, p-MDM2; (D) p-ATM, p-ATR, p-BRCA1, p-Chk2; (E) AKT, p-AKT, ERK, p-ERK, P38, p-P38, JNK, p-JNK. β-Actin was used as the loading control.

arrest and apoptosis.[48] Therefore, we checked the combined effect of FA-BSANPs and radiation on the expression of p53 and DNA damage-related proteins in Hela cells. As expected, compared with each treatment alone, Hela cells cotreated with FA-BSANPs and radiation increased the expression of phosphorylated status of p53 and DNA damage-associated proteins such as p-Histone H2A.X, p-ATM, p-ATR and p-BRCA1, while they down-regulated the expression of phosphorylated MDM2, a p53-antagonistic protein (Figure 8C,D). These results above indicated that DNA damage-linked p53 activation was involved in G2/M phase arrest and apoptotic signaling pathways for FA-BSANPs-triggered radiosensitization.

AKT and MAPKs pathways play important roles for the cell cycle progression and can be activated by a variety of cellular stresses such as oxidative stimuli, radiation and growth factors.[49] Studies have supported the involvement of AKT and ERK pathways in the anticancer actions of radiation.[50−52] To understand whether AKT and MAPKs have an effect on combined treatment-caused G2/M phase arrest and apoptosis, we detected the AKT and MAPKs expression in treated Hela cells. As illustrated in Figure 8E, 8 Gy radiation alone decreased the expression of phosphorylated AKT and ERK. With the pretreatment of FA-BSANPs, phosphorylation of AKT and ERK were significantly inhibited, with no change in their total proteins observed. Moreover, the combined treatments also increased the phosphorylated status of pro-apoptotic kinase JNK, while demonstrated no effect on p38. Taken together, our results suggest that 8 Gy radiation alone can possibly inhibit AKT and ERK pathways, but activate other pro-survival signals (such as XRCC-1 and VEGF/VEGFR2) to antagonize cell death and enhance radioresistance. However, the combined treatment reversed the radioresistance of Hela cells by augmenting both G2/M phase arrest and apoptotic signaling pathways and enhanced the therapeutic effects of cervical cancer (Figure 8A).

CONCLUSION

In conclusion, this study demonstrated an efficient radiosensitizing method by using FA-conjugated BSANPs carrying selenocompound PSeD. FA, as a targeting ligand, significantly enhanced selectivity of the nanoparticles between cancer and normal cells. Moreover, under X-ray radiation, the cell adherence and cellular uptake of FA-BSANPs were significantly increased, due to the increase of nanoparticle surface roughness. FA-BSANPs in combination with X-ray synergistically enhanced intracellular ROS generation through nanoparticulate interfacial effect. Internalized FA-BSANPs inhibited radioresistance by suppressing the function of VEGF/VEGFR2, XRCC-1 and finally triggered G2/M phase arrest and apoptotic signaling pathways. This biocompatible and tumor-targeting drug delivery nanosystem can be used to overcome cancer radioresistance.

ASSOCIATED CONTENT

Supporting Information

SEM image of FA-BSANPs; stability and size distribution of FA-BSANPs in aqueous and PBS solution; FT-IR spectra and of FA-BSANPs, PSeD and FA; FA competing assay; localization of FA-BSANPs in Hela and L02 cells; combined treatment of FA-BSANPs and radiation enhanced growth inhibition in Hela cells using MTT assay; In vitro cytotoxicity of FA-BSANPs associated with X-ray radiation against L02 cells detected by clonogenic assay; population distribution of Sub G1, G0/G1, S and G2/M phases in Hela cells with the combined treatment of FA-BSANPs and radiation; effects of FA-BSANPs in combination with X-ray radiation on the expression level of apoptotic and G2/M phase arrest-related proteins in L02 cells; size distribution of FA-BSANPs in aqueous solution with or without

radiation; release profiles of FA-BSANPs under X-ray radiation at pH 7.4 and pH 5.3 solutions; surface roughness of FA-BSANPs with or without X-ray radiation detected by AFM microscopy; intracellular ROS overproduction caused by FA-BSANPs and radiation using a DCFDA probe. This material is available free of charge via the Internet at http://pubs.acs.org.

AUTHOR INFORMATION

Corresponding Author

*Tianfeng Chen. E-mail: tchentf@jnu.edu.cn. Tel: +86 20-85225962. Fax: +86 20 85221263. Address: Room 643, Department of Chemistry, Jinan University, Guangzhou 510632, China.

Notes

The authors declare no competing financial interest.

ACKNOWLEDGMENTS

This work was supported by National High Technology Reach and Development Program of China (863 Program, SS2014AA020538), Science Foundation for Distinguished Young Scholars of Guangdong Province, Natural Science Foundation of China and Guangdong Province, Program for New Century Excellent Talents in University, Research Fund for the Doctoral Program of Higher Education of China and China Postdoctoral Science Foundation.

REFERENCES

(1) Lord, C. J.; Ashworth, A. The DNA Damage Response and Cancer Therapy. *Nature* **2012**, *481*, 287−294.

(2) Fan, W. P.; Shen, B.; Bu, W. B.; Chen, F.; Zhao, K. L.; Zhang, S. J.; Zhou, L. P.; Peng, W. J.; Xiao, Q. F.; Xing, H. Y.; Liu, J. N.; Ni, D. L.; He, Q. J.; Shi, J. L. Rattle-Structured Multifunctional Nanotheranostics for Synergetic Chemo-/Radiotherapy and Simultaneous Magnetic/Luminescent Dual-Mode Imaging. *J. Am. Chem. Soc.* **2013**, *135*, 6494−6503.

(3) Pan, Y.; Zhang, Q.; Atsaves, V.; Yang, H.; Claret, F. X. Suppression of Jab1/CSN5 Induces Radio- and Chemo-sensitivity in Nasopharyngeal Carcinoma Through Changes to the DNA Damage and Repair Pathways. *Oncogene* **2013**, *32*, 2756−2766.

(4) Beskow, C.; Skikuniene, J.; Holgersson, A.; Nilsson, B.; Lewensohn, R.; Kanter, L.; Viktorsson, K. Radioresistant Cervical Cancer Shows Upregulation of the NHEJ Proteins DNA-PKcs, Ku70 and Ku86. *Br. J. Cancer* **2009**, *101*, 816−821.

(5) Wang, M.; Morsbach, F.; Sander, D.; Gheorghiu, L.; Nanda, A.; Benes, C.; Kriegs, M.; Krause, M.; Dikomey, E.; Baumann, M.; Dahm-Daphi, J.; Settleman, J.; Willers, H. EGF Receptor Inhibition Radiosensitizes NSCLC Cells by Inducing Senescence in Cells Sustaining DNA Double-Strand Breaks. *Cancer Res.* **2011**, *71*, 6261−6269.

(6) Gu, J. L.; Su, S. S.; Li, Y. S.; He, Q. J.; Zhong, F. Y.; Shi, J. L. Surface Modification-Complexation Strategy for Cisplatin Loading in Mesoporous Nanoparticles. *J. Phys. Chem. Lett.* **2010**, *1*, 3446−3450.

(7) Werner, M. E.; Copp, J. A.; Karve, S.; Cummings, N. D.; Sukumar, R.; Li, C. X.; Napier, M. E.; Chen, R. C.; Cox, A. D.; Wang, A. Z. Folate-Targeted Polymeric Nanoparticle Formulation of Docetaxel Is an Effective Molecularly Targeted Radiosensitizer with Efficacy Dependent on the Timing of Radiotherapy. *ACS Nano* **2011**, *5*, 8990−8998.

(8) Corde, S.; Balosso, J.; Elleaume, H.; Renier, M.; Joubert, A.; Biston, M. C.; Adam, J. F.; Charvet, A. M.; Brochard, T.; Le Bas, J. F.; Esteve, F.; Foray, N. Synchrotron Photoactivation of Cisplatin Elicits an Extra Number of DNA Breaks that Stimulate RAD51-Mediated Repair Pathways. *Cancer Res.* **2003**, *63*, 3221−3227.

(9) Sinha, R.; El-Bayoumy, K. Apoptosis Is a Critical Cellular Event in Cancer Chemoprevention and Chemotherapy by Selenium Compounds. *Curr. Cancer Drug Targets* **2004**, *4*, 13−28.

(10) Li, S.; Zhou, Y.; Wang, R.; Zhang, H.; Dong, Y.; Ip, C. Selenium Sensitizes MCF-7 Breast Cancer Cells to Doxorubicin-Induced Apoptosis Through Modulation of Phospho-AKT and Its Downstream Substrates. *Mol. Cancer Ther.* **2007**, *6*, 1031−1038.

(11) Chen, T.; Wong, Y. S.; Zheng, W.; Liu, J. Caspase- and p53-Dependent Apoptosis in Breast Carcinoma Cells Induced by a Synthetic Selenadiazole Derivative. *Chem.-Biol. Interact.* **2009**, *180*, 54−60.

(12) Chen, T.; Wong, Y. S. Selenocystine Induces S-Phase Arrest and Apoptosis in Human Breast Adenocarcinoma MCF-7 Cells by Modulating ERK and AKT Phosphorylation. *J. Agric. Food Chem.* **2008**, *56*, 10574−10581.

(13) Luo, Y.; Li, X.; Huang, X.; Wong, Y. S.; Chen, T.; Zhang, Y.; Zheng, W. 1,4-Diselenophene-1,4-diketone Triggers Caspase-Dependent Apoptosis in Human Melanoma A375 Cells through Induction of Mitochondrial Dysfunction. *Chem. Pharm. Bull.* **2013**, *59*, 1227−1232.

(14) Luo, Y.; Li, X. L.; Chen, T. F.; Wang, Y.; Zheng, W. J. Synthesis of a Novel Thiophene Derivative that Induces Cancer Cell Apoptosis Through Modulation of AKT and MAPK Pathways. *MedChemComm* **2012**, *3*, 1143−1146.

(15) Liu, X.; Law, W. C.; Jeon, M.; Wang, X.; Liu, M.; Kim, C.; Prasad, P. N.; Swihart, M. T. Cu2-x Se Nanocrystals with Localized Surface Plasmon Resonance as Sensitive Contrast Agents for in Vivo Photoacoustic Imaging: Demonstration of Sentinel Lymph Node Mapping. *Adv. Healthcare Mater.* **2013**, *2*, 952−957.

(16) Barrow, S. J.; Funston, A. M.; Wei, X. Z.; Mulvaney, P. DNA-Directed Self-Assembly and Optical Properties of Discrete 1D, 2D and 3D Plasmonic Structures. *Nano Today* **2013**, 8138−8167.

(17) Luo, Z.; Ding, X. W.; Hu, Y.; Wu, S. J.; Xiang, Y.; Zeng, Y. F.; Zhang, B. L.; Yan, H.; Zhang, H. C.; Zhu, L. L.; Liu, J. J.; Li, J. H.; Cai, K. Y.; Zhao, Y. L. Engineering a Hollow Nanocontainer Platform with Multifunctional Molecular Machines for Tumor-Targeted Therapy in Vitro and in Vivo. *ACS Nano* **2013**, *7*, 10271−10284.

(18) Kakuta, T.; Takashima, Y.; Nakahata, M.; Otsubo, M.; Yamaguchi, H.; Harada, A. Preorganized Hydrogel: Self-Healing Properties of Supramolecular Hydrogels Formed by Polymerization of Host-Guest-Monomers that Contain Cyclodextrins and Hydrophobic Guest Groups. *Adv. Mater.* **2013**, *25*, 2849−2853.

(19) Peng, L.; Peng, X.; Liu, B.; Wu, C.; Xie, Y.; Yu, G. Ultrathin Two-Dimensional MnO2/Graphene Hybrid Nanostructures for High-Performance, Flexible Planar Supercapacitors. *Nano Lett.* **2013**, *13*, 2151−2157.

(20) Caracciolo, G.; Cardarelli, F.; Pozzi, D.; Salomone, F.; Maccari, G.; Bardi, G.; Capriotti, A. L.; Cavaliere, C.; Papi, M.; Lagana, A. Selective Targeting Capability Acquired with a Protein Corona Adsorbed on the Surface of 1,2-Dioleoyl-3-trimethylammonium Propane/DNA Nanoparticles. *ACS Appl. Mater. Interfaces* **2013**, *5*, 13171−13179.

(21) Zhao, M. X.; Hu, B. L.; Gu, Z.; Joo, K. I.; Wang, P.; Tang, Y. Degradable Polymeric Nanocapsule for Efficient Intracellular Delivery of a High Molecular Weight Tumor-Selective Protein Complex. *Nano Today* **2013**, *8*, 11−20.

(22) Taratula, O.; Kuzmov, A.; Shah, M.; Garbuzenko, O. B.; Minko, T. Nanostructured Lipid Carriers as Multifunctional Nanomedicine Platform for Pulmonary Co-Delivery of Anticancer Drugs and siRNA. *J. Controlled Release* **2013**, *171*, 349−357.

(23) Park, S.; Kang, S.; Chen, X. Y.; Kim, E. J.; Kim, J.; Kim, N.; Kim, J.; Jin, M. M. Tumor Suppression via Paclitaxel-Loaded Drug Carriers that Target Inflammation Marker Upregulated in Tumor Vasculature and Macrophages. *Biomaterials* **2013**, *34*, 598−605.

(24) Kratz, F. Albumin as a Drug Carrier: Design of Prodrugs, Drug Conjugates and Nanoparticles. *J. Controlled Release* **2008**, *132*, 171−183.

(25) Heukers, R.; Altintas, I.; Raghoenath, S.; De Zan, E.; Pepermans, R.; Roovers, R. C.; Haselberg, R.; Hennink, W. E.; Schiffelers, R. M.; Kok, R. J.; Henegouwen, P. M. P. V. B. E. Targeting Hepatocyte Growth Factor Receptor (Met) Positive Tumor Cells Using Internalizing Nanobody-Decorated Albumin Nanoparticles. *Biomaterials* **2014**, *35*, 601−610.

(26) Zhang, S. F.; Kucharski, C.; Doschak, M. R.; Sebald, W.; Uludag, H. Polyethylenimine-PEG Coated Albumin Nanoparticles for BMP-2 Delivery. *Biomaterials* **2010**, *31*, 952−963.
(27) Mohanta, V.; Madras, G.; Patil, S. Layer-by-Layer Assembled Thin Film of Albumin Nanoparticles for Delivery of Doxorubicin. *J. Phys. Chem. C* **2012**, *116*, 5333−5341.
(28) Xie, L. L.; Tong, W. J.; Yu, D. H.; Xu, J. Q.; Li, J.; Gao, C. Y. Bovine Serum Albumin Nanoparticles Modified with Multilayers and Aptamers for pH-Responsive and Targeted Anti-Cancer Drug Delivery. *J. Mater. Chem.* **2012**, *22*, 6053−6060.
(29) Bae, S.; Ma, K.; Kim, T. H.; Lee, E. S.; Oh, K. T.; Park, E. S.; Lee, K. C.; Youn, Y. S. Doxorubicin-Loaded Human Serum Albumin Nanoparticles Surface-Modified with TNF-Related Apoptosis-Inducing Ligand and Transferrin for Targeting Multiple Tumor Types. *Biomaterials* **2012**, *33*, 1536−1546.
(30) Destito, G.; Yeh, R.; Rae, C. S.; Finn, M. G.; Manchester, M. Folic Acid-Mediated Targeting of Cowpea Mosaic Virus Particles to Tumor Cells. *Chem. Biol.* **2007**, *14*, 1152−1162.
(31) Harada, H.; Kizaka-Kondoh, S.; Li, G.; Itasaka, S.; Shibuya, K.; Inoue, M.; Hiraoka, M. Significance of HIF-1-Active Cells in Angiogenesis and Radioresistance. *Oncogene* **2007**, *26*, 7508−7516.
(32) Iftner, T.; Elbel, M.; Schopp, B.; Hiller, T.; Loizou, J. I.; Caldecott, K. W.; Stubenrauch, F. Interference of Papillomavirus E6 Protein with Single-Strand Break Repair by Interaction with XRCC1. *EMBO J.* **2002**, *21*, 4741−4748.
(33) Franken, N. A.; Rodermond, H. M.; Stap, J.; Haveman, J.; van Bree, C. Clonogenic Assay of Cells in Vitro. *Nat. Protoc.* **2006**, *1*, 2315−2319.
(34) Chen, T. F.; Wong, Y. S. Selenocystine Induces Reactive Oxygen Species-Mediated Apoptosis in Human Cancer Cells. *Biomed. Pharmacother.* **2009**, *63*, 105−113.
(35) Huang, Y.; He, L.; Liu, W.; Fan, C.; Zheng, W.; Wong, Y. S.; Chen, T. Selective Cellular Uptake and Induction of Apoptosis of Cancer-Targeted Selenium Nanoparticles. *Biomaterials* **2013**, *34*, 7106−7116.
(36) Chen, T. F.; Wong, Y. S. Selenocystine Induces Caspase-Independent Apoptosis in MCF-7 Human Breast Carcinoma Cells with Involvement of p53 Phosphorylation and Reactive Oxygen Species Generation. *Int. J. Biochem. Cell Biol.* **2009**, *41*, 666−676.
(37) Nagata, S. Apoptosis by Death Factor. *Cell.* **1997**, *88*, 355−365.
(38) Thorburn, A. Death Receptor-Induced Cell Killing. *Cell Signalling* **2004**, *16*, 139−44.
(39) Aggarwal, B. B. Signalling Pathways of the TNF Superfamily: A Double-Edged Sword. *Nat. Rev. Immunol.* **2003**, *3*, 745−756.
(40) Hengartner, M. O. The Biochemistry of Apoptosis. *Nature* **2000**, *407*, 770−776.
(41) Tay, C. Y.; Fang, W.; Setyawati, M. I.; Chia, S. L.; Tan, K. S.; Hong, C. H.; Leong, D. T. Nano-Hydroxyapatite and Nano-Titanium Dioxide Exhibit Different Subcellular Distribution and Apoptotic Profile in Human Oral Epithelium. *ACS Appl. Mater. Interfaces* **2014**, *6*, 6248−6256.
(42) Tsukamoto, H.; Shibata, K.; Kajiyama, H.; Terauchi, M.; Nawa, A.; Kikkawa, F. Aminopeptidase N (APN)/CD13 Inhibitor, Ubenimex, Enhances Radiation Sensitivity in Human Cervical Cancer. *BMC Cancer* **2008**, *8*, 1−8.
(43) Kim, J. G.; Bae, J. H.; Kim, J. A.; Heo, K.; Yang, K.; Yi, J. M. Combination Effect of Epigenetic Regulation and Iionizing Radiation in Colorectal Cancer Cells. *PloS one* **2014**, *9*, 1−10.
(44) Pelicano, H.; Carney, D.; Huang, P. ROS Stress in Cancer Cells and Therapeutic Implications. *Drug Resist. Updates* **2004**, *7*, 97−110.
(45) Zhang, X. D.; Luo, Z.; Chen, J.; Shen, X.; Song, S.; Sun, Y.; Fan, S.; Fan, F.; Leong, D. T.; Xie, J. Ultrasmall Au(10-12)(SG)(10-12) Nanomolecules for High Tumor Specificity and Cancer Radiotherapy. *Adv. Mater.* **2014**, *26*, 4565−4568.
(46) Zhang, X. D.; Chen, J.; Luo, Z.; Wu, D.; Shen, X.; Song, S. S.; Sun, Y. M.; Liu, P. X.; Zhao, J.; Huo, S.; Fan, S.; Fan, F.; Liang, X. J.; Xie, J. Enhanced Tumor Accumulation of Sub-2 nm Gold Nanoclusters for Cancer Radiation Therapy. *Adv. Healthcare Mater.* **2014**, *3*, 133−141.
(47) Horie, M.; Kato, H.; Fujita, K.; Endoh, S.; Iwahashi, H. In Vitro Evaluation of Cellular Response Induced by Manufactured Nanoparticles. *Chem. Res. Toxicol.* **2013**, *25*, 605−619.
(48) Setyawati, M. I.; Yuan, X.; Xie, J.; Leong, D. T. The Influence of Lysosomal Stability of Silver Nanomaterials on Their Toxicity to Human Cells. *Biomaterials* **2013**, *35*, 6707−6715.
(49) Raingeaud, J.; Gupta, S.; Rogers, J. S.; Dickens, M.; Han, J.; Ulevitch, R. J.; Davis, R. J. Pro-Inflammatory Cytokines and Environmental Stress Cause p38 Mitogen-Activated Protein Kinase Activation by Dual Phosphorylation on Tyrosine and Threonine. *J. Biol. Chem.* **1995**, *270*, 7420−7426.
(50) Nam, S. Y.; Seo, H. H.; Park, H. S.; An, S.; Kim, J. Y.; Yang, K. H.; Kim, C. S.; Jeong, M.; Jin, Y. W. Phosphorylation of CLK2 at Serine 34 and Threonine 127 by AKT Controls Cell Survival After Ionizing Radiation. *J. Biol. Chem.* **2010**, *285*, 31157−31163.
(51) Xia, S.; Zhao, Y.; Yu, S.; Zhang, M. Activated PI3K/AKT/COX-2 Pathway Induces Resistance to Radiation in Human Cervical Cancer Hela Cells. *Cancer Biother. Radiopharm.* **2010**, *25*, 317−323.
(52) Fritz, G.; Brachetti, C.; Kaina, B. Lovastatin Causes Sensitization of Hela Cells to Ionizing Radiation-Induced Apoptosis by The Abrogation of G2 Blockage. *Int. J. Radiat. Biol.* **2003**, *79*, 601−610.